Vibrational coherence transfer in the ultrafast intersystem crossing of a diplatinum complex in solution

Roberto Monni[a], Gloria Capano[a], Gerald Auböck[a,1], Harry B. Gray[b], Antonín Vlček[c,d], Ivano Tavernelli[e], and Majed Chergui[a,2]

[a]Laboratoire de Spectroscopie Ultrarapide, Lausanne Centre for Ultrafast Science, Institut des Sciences et Ingénierie Chimiques, School of Basic Sciences, Ecole Polytechnique Fédérale de Lausanne, CH-1015 Lausanne, Switzerland; [b]Beckman Institute, California Institute of Technology, Pasadena, CA 91125; [c]School of Biological and Chemical Sciences, Queen Mary University of London, London E1 4NS, United Kingdom; [d]J. Heyrovský Institute of Physical Chemistry, Czech Academy of Sciences, CZ-182 23 Prague, Czech Republic; and [e]Science & Technology Department, IBM Research GmbH, Zurich Research Laboratory, 8803 Rüschlikon, Switzerland

Edited by Martin Gruebele, University of Illinois at Urbana–Champaign, Urbana, IL, and approved June 1, 2018 (received for review November 23, 2017)

We investigate the ultrafast transient absorption response of tetrakis(μ-pyrophosphito)diplatinate(II), $[Pt_2(\mu\text{-}P_2O_5H_2)_4]^{4-}$ [hereafter abbreviated Pt(pop)], in acetonitrile upon excitation of its lowest singlet $^1A_{2u}$ state. Compared with previously reported solvents [van der Veen RM, Cannizzo A, van Mourik F, Vlček A, Jr, Chergui M (2011) *J Am Chem Soc* 133:305–315], a significant shortening of the intersystem crossing (ISC) time (<1 ps) from the lowest singlet to the lowest triplet state is found, allowing for a transfer of vibrational coherence, observed in the course of an ISC in a polyatomic molecule in solution. Density functional theory (DFT) quantum mechanical/molecular mechanical (QM/MM) simulations of Pt(pop) in acetonitrile and ethanol show that high-lying, mostly triplet, states are strongly mixed and shifted to lower energies due to interactions with the solvent, providing an intermediate state (or manifold of states) for the ISC. This suggests that the larger the solvation energies of the intermediate state(s), the shorter the ISC time. Because the latter is smaller than the pure dephasing time of the vibrational wave packet, coherence is conserved during the spin transition. These results underscore the crucial role of the solvent in directing pathways of intramolecular energy flow.

ultrafast | intersystem crossing | vibrational coherence | diplatinum complexes | solvation

Vibrational and electronic energy flows play a crucial role in photochemistry and photobiology, and their identification is essential for understanding nature and for applications such as solar energy conversion, photocatalysis, phototherapy, and luminescent materials. With the advent of femtosecond laser spectroscopy, it has become possible to track the timescales and pathways of energy relaxation in complex systems (1, 2). In particular, the observation of vibrational quantum beats (wave packets) has become commonplace (3–12). Wave packets reflect spatial localization of the nuclei at a given instant in a specific mode, reflecting coherent behavior. In the condensed phase, wave packets can be damped via elastic and inelastic dephasing processes by collisions with solvent molecules. In the former case, the phase relationship of the vibrational wave functions making up the wave packet is destroyed without a change of the vibrational energy, while in the inelastic case, the energies of the vibrational levels do change. Furthermore, when the electronic state onto which the wave packet is evolving is coupled to another electronic state or a photoproduct, population transfers can occur with retention of the vibrational coherence (4). In this case, the wave packet in the initial state will gradually lose amplitude after each oscillation, and detection of wave packets in product states delivers information about relaxation pathways and their timescales, couplings between states and the vibrational modes that may be involved in the electronic energy flow and/or chemical transformation.

Transfer of vibrational coherence between two electronic states was first observed in the gaseous NaI molecule (4, 12). A gradual damping of the wave packet amplitude in the initially excited bound state was accompanied by a pulse-like generation of Na atomic fragments upon each passage of the wave packet at the point of crossing with the lowest, purely dissociative excited state (ES). For polyatomic molecules and biological chromophores in a dissipative environment (solvent or protein), vibrational wave packets have mostly been observed either in the final populated ES and/or the ground state (GS) [formed via impulsive stimulated Raman scattering (13) or via an ultrafast nonradiative relaxation from an ES], or the product state. Examples are found in ultrafast photodissociation reactions, where a molecular fragment carries away internal vibrational and/or rotational energy in a coherent fashion (10, 14–19). In these cases, the coherences are reaction driven, that is, they are generated as a result of impulsive motion along a specific coordinate, as opposed to field driven, where they are directly generated by the laser pulse (17). Observation of wave packets has been reported in the lowest ES resulting, for example, from ES twisting and charge separation processes in tetraphenylethylene in solution (20), isomerization of the retinal chromophore in its protein pocket (21–24) and in solutions (25), isomerization of photoswitches (26), ultrafast ES intramolecular proton transfer in solution (27), internal conversion in dye molecules (28, 29),

Significance

The observation of vibrational wave packets allows tracking the pathways of energy relaxation in nonadiabatic surface crossing events of (bio)molecular systems, such as conical intersections or charge transfer processes. Here, we identify transfer of vibrational coherence in the course of conversion between electronic excited states of different spin in a diplatinum complex in solution, as an example. Retention of coherence is due to the fact that the conversion rate is dramatically accelerated in an acetonitrile solvent due to the strong solvation of higher-lying electronic states that then provide the channel for the coherent population flow from the singlet to the triplet state. These results highlight the role of the environment in controlling the pathways of energy flow and conversion.

Author contributions: M.C. designed research; R.M., G.C., G.A., and I.T. performed research; G.C., H.B.G., and I.T. contributed new reagents/analytic tools; R.M., G.C., G.A., A.V., I.T., and M.C. analyzed data; and M.C. wrote the paper.

The authors declare no conflict of interest.

This article is a PNAS Direct Submission.

[1]Present address: Department of Photonic Systems, CTR Carinthian Tech Research AG, 9524 Villach/St. Magdalen, Austria.

[2]To whom correspondence should be addressed. Email: majed.chergui@epfl.ch.

This article contains supporting information online at www.pnas.org/lookup/suppl/doi:10.1073/pnas.1719899115/-/DCSupplemental.

Published online June 25, 2018.

intramolecular charge transfer excitation in plastocyanin (30, 31), and electron transfer in molecular complexes (32). Molecular dynamics (MD) simulations with quantum transitions involving 14 potential surfaces, of the population relaxation in the Hg_2 molecule in a low-temperature argon matrix, have also concluded that vibrational coherence can be conserved over multiple nonadiabatic curve crossing events (33).

Vibrational wave packets were also detected in the final states of ultrafast intersystem crossing (ISC) events in $[Fe(bpy)_3]^{2+}$ complexes (34, 35), $Cr(acac)_3$ (36), $[Au(CN)^{2-}]_3$ trimers (37), and $[Au(CN)^{2-}]_2$ dimers (38). The case of the much-studied $[Fe(bpy)_3]^{2+}$ complex is striking because the photoinduced spin crossover (SCO) therein involves an ultrafast relaxation from the initially excited (singlet) state(s) to the lowest quintet state, showing a rich pattern of vibrational wave packets in the high-spin state, independent of excitation energy (34, 35, 39). In this case, the coherences were attributed to the impulsive population of the quintet state, which implies an elongation of the Fe–N bonds. In $Cr(acac)_3$, a population was found to appear in the low-spin doublet final state after excitation of the high-spin quartet state (36). The ISC and the transfer of coherence between the two states were based on geometric changes. A 70-fs decoherence time was reported, which was attributed to the ISC time. However, the vibrational coherences only show up in the product doublet state, and the optically populated quartet state was not detected. Therefore, transfer of coherence during ISC is inferred but not directly observed. In the case of $[Au(CN)^{2-}]_3$ (37) and $[Au(CN)^{2-}]_2$ (38), coherences due to the impulsive Au–Au bond shortening upon excitation, were observed in a mechanism similar to what was reported for the $[Pt_2(\mu\text{-}P_2O_5H_2)_4]^{4-}$ complex in solution (40). In these trimers and dimers, the coherences appeared only in the final triplet state after excitation of a singlet state. This is most likely due to the fact that the Au–Au oscillation (~400 fs) cannot be completed in the singlet states due to the ISC time of ~240 fs.

Thus, none of the above examples, and regardless of the nature of the coupling between the electronic states, demonstrates field-driven wave packets in the initially excited state that are then coherently transferred to the final state of different spin in an ISC event. The alternative, reaction-driven scenario, would be the impulsive decay of high-frequency mode(s) in the initially excited state, which then generate low-frequency wave packets in the final state. Indeed, it was theoretically predicted by Jean and Fleming (41) that, for a harmonic well, energy relaxation can occur with retention of the vibrational phase and that, for a sufficiently strong electronic coupling, the product of an electronic curve crossing process can be formed vibrationally coherent even when no coherence is present in the initially excited state.

To address the issue of conservation of vibrational coherence in ISC events, a class of polyatomic molecules has recently emerged that exhibits clear and rich patterns of vibrational coherence. Bimetallic d^8–d^8 complexes of Pt^{II}, Rh^{I}, and Ir^{I} ions undergo a metal–metal bond formation in their lowest singlet and triplet ESs, due to the fact that the HOMO has dσ-antibonding (dσ*) character and the LUMO has pσ-bonding character, which leads to a shortening of the metal–metal equilibrium distance (42). A case in point is the tetrakis(μ-pyrophosphito)diplatinate(II), $[Pt_2(\mu\text{-}P_2O_5H_2)_4]^{4-}$ complex, hereafter abbreviated Pt(pop), where the two Pt^{II} atoms are in a square-planar coordination geometry linked by four P–O–P bridges that encage the Pt–Pt moiety and shield it from the environment, except for the open axial sites (Fig. 1). A Pt–Pt contraction of 0.21–0.31 Å relative to the GS was determined for the lowest $^3A_{2u}$ (T_1) and the $^1A_{2u}$ (S_1) states (in the D_{4h} symmetry of the Pt_2P_8 core) of Pt(pop) using high-resolution low-temperature steady-state optical spectroscopy (43–45), and more recently, time-resolved X-ray absorption spectroscopy (46, 47) and X-ray scattering (48).

Exploiting the bond-forming dσ* → pσ transition, van der Veen et al. (40) demonstrated that vibrational wave packets of the Pt–Pt bond could be generated in the S_1 state upon impulsive excitation by a femtosecond pulse. The encapsulated Pt–Pt moiety was found to behave as a quasiharmonic oscillator, up to at least the 20th overtone, consistent with the low-temperature high-resolution optical studies (45). A solvent-independent dephasing time of ~2–2.5 ps was measured (40). This first demonstration of wave packet dynamics upon impulsive bond formation was followed by observation of coherent oscillations in Pt_2 complexes with metal–metal-to-ligand charge transfer lowest ESs (49), and in an Ir_2 complex (50). More recently, we investigated the relaxation dynamics of Pt(pop) in solution upon excitation of the UV bands lying above the S_1 state and found that the T_1 electronic state is directly and promptly populated, exhibiting a rich vibrational wave packet pattern (51). Clearly, an ultrafast relaxation channel that bypasses the S_1 state is present.

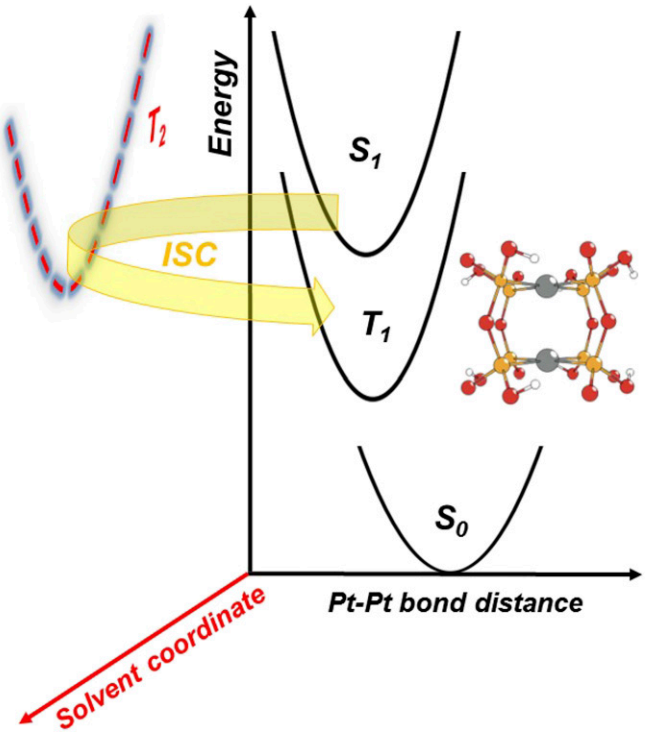

Fig. 1. Schematic structure of the molecule and a potential curve diagram along the Pt–Pt coordinate showing the ground and the lowest singlet and triplet excited states. The red dashed curve schematically represents the T_2 state that mediates the ISC. The blurring of this curve is meant to show that its position depends on the solvent.

The molecular parameters (equilibrium distance, vibrational frequency) of the ground S_0 ($^1A_{1g}$) and lowest two excited (S_1 and T_1) states of Pt(pop) are given in *SI Appendix*, Table S1. The S_1 and T_1 states (separated by ~5,000 cm^{-1}; *SI Appendix*, Table S2) have very close oscillation frequencies and equilibrium distances, and therefore nearly parallel potential curves along the Pt–Pt coordinate (Fig. 1). Direct spin–orbit coupling (SOC) between them is symmetry-forbidden, yet despite this: (*i*) ISC occurs with near-unity quantum yield (43) from the S_1 to the long-lived (8–10 μs) T_1 state (52); (*ii*) the ISC rate is solvent dependent, and its time constant spans from ~10 ps to tens of picoseconds (*SI Appendix*, Table S2) (40, 53). This marked solvent dependence is surprising since the SOC is an intrinsic property of the molecule.

Here, compared with previously studied solvents (40, 53), we find that a dramatic shortening of the ISC time occurs in the case of Pt(pop) in the acetonitrile solvent, which enables a clearcut transfer of vibrational coherence from the S_1 to the T_1 state. This first demonstration of an ISC-mediated transfer of vibrational coherence for a polyatomic molecule in solution is qualitatively rationalized by combined quantum mechanical/molecular mechanical (QM/MM) simulations with linear-response time-dependent density functional theory (LR-TDDFT). These calculations show that the higher-lying (predominantly triplet) ligand-to-metal-metal-charge-transfer

(LMMCT) states are strongly stabilized and mixed together, as well as with the low-lying dσ*–pσ states, by interactions with the solvent, bringing them to near resonance with the S_1 state and therefore providing the intermediate state(s) for the ultrafast ISC to the T_1 state.

Methods

The experimental procedures, setup, and data analysis are described in *SI Appendix*, sections SI and SII, and in refs. 39 and 54. Briefly, we excite the sample [a room temperature solution of Pt(pop) in acetonitrile] with 360-nm pump pulses having a typical bandwidth of ∼2 nm and energy of ∼150 nJ, focused into a 100-μm-diameter spot. The probe pulse is a white-light supercontinuum from ∼340 to ∼600 nm. After focusing it onto the sample (35-μm diameter at focal spot), it is coupled into a 100-μm multimode fiber and sent to a spectrometer to be spectrally resolved and detected on a single-shot basis by means of a fast complementary metal–oxide–semiconductor array detector. The pump pulses are chopped at one-half the laser repetition rate, which is also that of the probe pulses.

The computational methods are described in *SI Appendix*, section SIII, and refs. 55–57. Briefly, we use an explicit solvent model by performing ab initio MD simulations within the QM/MM framework. The quantum box contains a Pt(pop) molecule (38 atoms), while the classical box includes four Na^+ ions for balancing the negative charge of Pt(pop) and 1,624 MeCN molecules. The electronic energy was computed using B3LYP exchange and correlation functional with dispersion-corrected atom-centered potentials correction (58–60) for dispersion forces. In addition, SOC between all excited singlet and triplet states has been computed at the same steps using the Wang–Ziegler formalism (61) as implemented in the Amsterdam density functional code. Since the T_1 state and the photoexcited S_1 state have the same symmetry and their potential energy surfaces are nearly parallel, the forces acting on the nuclei are almost identical in both cases. This means that we can perform a Born–Oppenheimer MD simulation on the T_1 state, which also reflects the dynamics on the S_1 state. This considerably reduces the computational cost and makes the ES dynamics study of Pt(pop) feasible.

Results and Discussion

The UV-visible absorption spectra of Pt(pop) dissolved in different solvents are shown in *SI Appendix*, Fig. S1. They display spectral features due to the dσ* → pσ transition: an intense dipole-allowed $S_0 \rightarrow S_1$ band centered around 360–370 nm, and a weak $S_0 \rightarrow T_1$ band around 440–460 nm (44, 45, 52, 62, 63). The region below 320 nm shows three bands (*SI Appendix*, Fig. S1, arrows) that are more solvent sensitive than the lower-lying dσ* → pσ transitions. These bands are notably weaker than the singlet $S_0 \rightarrow S_1$ band, but about 5–10 times stronger than the $S_0 \rightarrow T_1$ transition, pointing to a partial dipole- and/or spin-forbidden character. The nature of the UV bands was recently addressed by Záliš et al. (62), using spin–orbit TDDFT with an implicit solvent. They concluded that these bands involve transitions from lower-lying predominantly ligand-localized molecular orbitals to the LUMO, which can be approximately described as LMMCT states, all having a predominantly triplet character, with some singlet contribution (*SI Appendix*, Table S2, bottom row). The UV range additionally contains a manifold of states with negligible oscillator strengths from the GS (62).

Fig. 2*A* shows a time–wavelength (t–λ) plot of the transient absorption of Pt(pop) in MeCN upon excitation at 360 nm into the blue wing of the $S_0 \rightarrow S_1$ band (*SI Appendix*, Fig. S1). It shows several positive and negative signals, with rich oscillatory patterns on them. These oscillations are due to vibrational wave packets in the GS and ESs, as discussed below. Cuts at fixed time delays yield the transient spectra, shown in Fig. 2*B*, while those at fixed wavelengths yield the time traces shown in Fig. 3 and *SI Appendix*, Fig. S2.

Based on our previous studies in other solvents (40, 51) and on the molecular parameters of the S_0, S_1, and T_1 states (*SI Appendix*, Table S1), the assignment of the various features in Fig. 2 is straightforward: (*i*) the negative signal in the ∼360- to 390-nm region is due to the GS bleach (GSB) as this is where the GS singlet absorption band lies (*SI Appendix*, Fig. S1). This is further confirmed by the time traces at 371 and 379 nm (*SI Appendix*, Fig. S2), which show a clear oscillatory pattern due to a vibrational wave packet of the Pt–Pt stretch mode in the GS (∼120 cm^{-1}; *SI Appendix*, Table S1). This wave packet is generated by impulsive stimulated Raman scattering as previously reported (40); (*ii*) the negative signal in the ∼390- to 430-nm region corresponds to stimulated emission (SE) from the S_1 state. Indeed, this is where the fluorescence from this state was reported in other solvents (40). It shows a clear damped oscillatory pattern (see the 411-nm trace in Fig. 3), with a frequency of 150 cm^{-1}, which is typical of the S_1 state as extracted from low-temperature steady-state spectroscopic studies (40, 44, 45). The oscillation amplitude decreases significantly over ∼1 ps; (*iii*) in ref. 40, the ES absorption (ESA_S) of

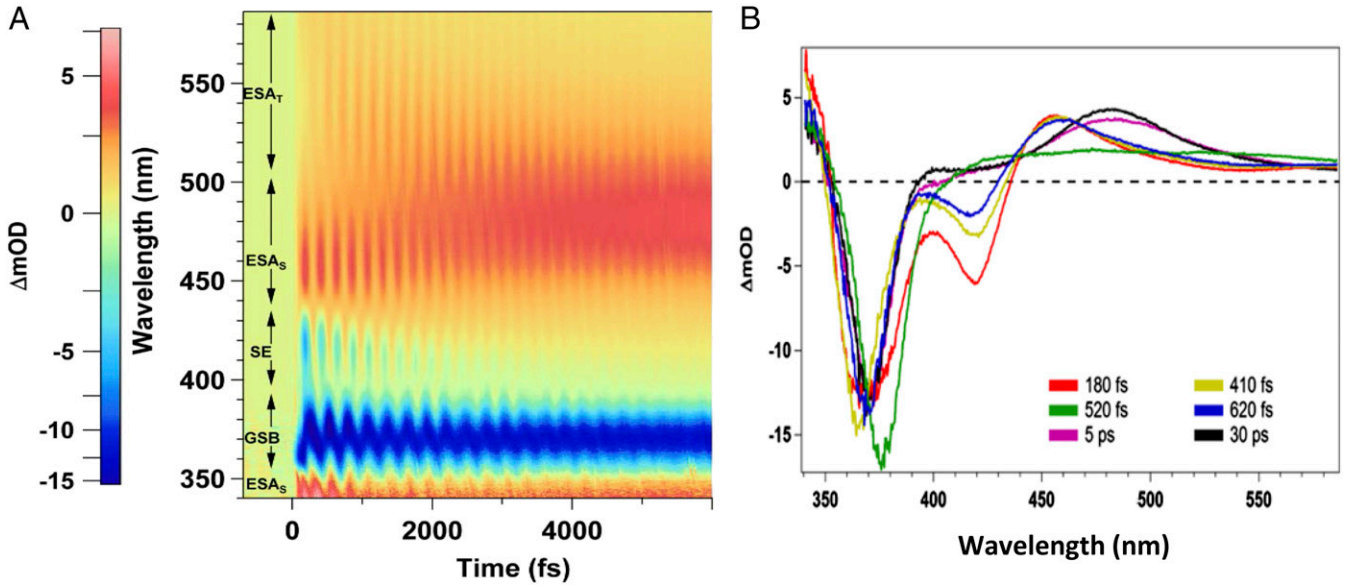

Fig. 2. Time–wavelength plots of Pt(pop) in MeCN upon 360-nm excitation (*A*) and corresponding transients spectra at different time delays (*B*). The minimum around 360–380 nm is due to the GS bleach (GSB), and that around 420 nm is due to stimulated emission (SE) of the S_1 state, while the maximum around 450 nm is due to its ES absorption (ESA). Finally, the maximum around 480 nm is due to the ESA of the T_1 state (see *Results and Discussion* for a detailed assignment). The traces in the first 0.6 ps show variations in position and amplitude due to the fact that the cuts are taken in the region where the wave packet oscillations occur.

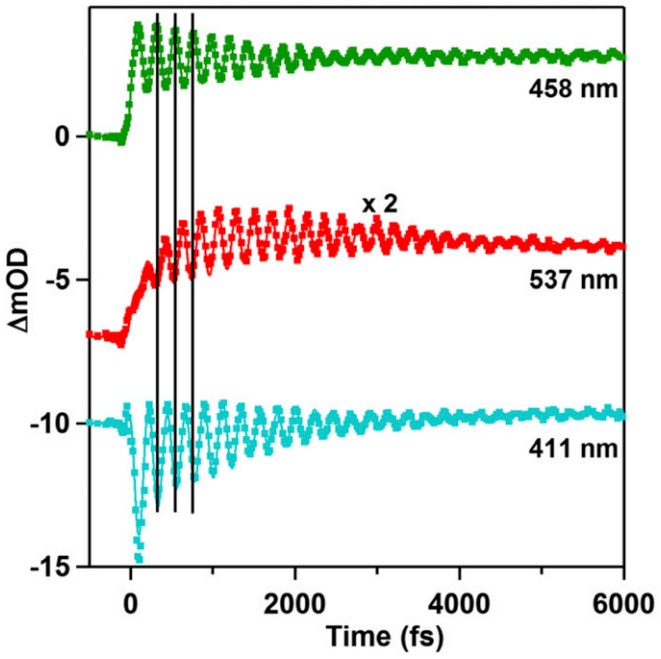

Fig. 3. Time traces of the signal upon 360-nm excitation of Pt(pop) in MeCN at selected wavelengths characteristic of the singlet state SE (411 nm) and ESA (458 nm) and the triplet ESA (537 nm). The solid lines show results of the global fit with the model described in *SI Appendix*, section SI.3.

the S_1 state appeared in the 430–480 nm region. In Fig. 2*A*, we indeed find a region of positive signal, which exhibits an oscillatory pattern with the same frequency, phase, and damping as the SE signal (compare traces at 411 and 458 nm in Fig. 3 and *SI Appendix*, Fig. S2); (*iv*) in ref. 51, the ESA of the T_1 state was clearly visible in the 450- to 550-nm region along with its oscillatory pattern at a frequency of ∼157 cm^{-1} (*SI Appendix*, Table S1). In Fig. 2, the region >500 nm shows a positive signal with an oscillatory pattern that grows in amplitude during the first picoseconds. This is clearly seen on the 537-nm trace of Fig. 3, which exhibits the frequency typical of the T_1 state. The growth of the absorption and oscillation amplitude in the latter, concomitant with the decay of the oscillations in the S_1 state, imply that population flows from the S_1 state to the T_1 state (Fig. 3), along with a transfer of vibrational coherence in the course of an ultrafast ISC. The further damping of the oscillations in the triplet state is due to dephasing as we discuss below. Coming to Fig. 2*B*, the various transient spectra therein displayed for $t < 1$ ps have strongly varying amplitudes and positions due to the fact that the cuts at the different time delays are affected by the oscillations. Once the oscillations have died away, the transient spectra at 5 and 30 ps contain only the GSB centered at 370 nm and the T_1 ESA centered at 470 nm. The narrowing of the latter between 5 and 30 ps is due to slow vibrational cooling.

In summary, the main differences between acetonitrile and the previously investigated solvents (40) is the prompt appearance and gradual decay of the S_1 state population (411- and 458-nm traces in Fig. 3), the concomitant rise of the T_1 state population, and the emergence of coherent oscillations in the T_1 state (537-nm trace). This reflects a significant acceleration of the ISC, since the signal of the T_1 state reaches its maximum amplitude by ∼1 ps. The SE trace at 411 nm is particularly interesting because it reflects the decay of the S_1 state population, analogous to what would be reported by spontaneous fluorescence (40). This probe wavelength samples the outer turning point of the S_1 state according to the steady-state fluorescence spectrum (40), with no overlap with other signals. It is therefore a neat representation of the wave packet evolving on the S_1 state, showing a clear damping of the amplitude.

We analyzed the datasets of Figs. 2 and 3 and *SI Appendix*, Fig. S2 by a global fit (GF) (for details, see *SI Appendix*, section SI.3). The function used to fit the entire set of time traces (*SI Appendix*, Eq. **S1**) is a sum of exponential terms (reflecting incoherent population kinetics) and damped (or growing) sine functions (reflecting coherent vibrational wave packet dynamics). The present data are best fitted with three exponential time constants (τ_1–τ_3), sine terms with frequencies due to the GS and the two ESs, along with their respective damping constants, either due to population decay, or to dephasing. The retrieved parameters are given in Table 1 and are compared with the results obtained upon 280-nm excitation, which only show the wave packet dynamics in the T_1 state (51). It is useful to note that those features, which reflect kinetic and dynamical signals of the T_1 state under 360-nm excitation, are in excellent agreement with those retrieved under 280-nm excitation, except for τ_1, which is a population time and should differ because of different population mechanisms. We extract exponential times of 700 ± 100 fs and 3.8 ± 0.4 ps (Table 1), while the oscillations in the S_1 state have the characteristic frequency of ∼150 cm^{-1} (40) and a damping time of 1.1 ± 0.1 ps. The 3.8 ± 0.4 ps is identical to the vibrational relaxation time in the triplet state derived from the results under 280-nm excitation. The parameters for the latter (e.g., see the 537-nm ESA_T trace) exhibits a gradual rise of its oscillation amplitude in 900 ± 100 fs at the characteristic frequency of ∼157 cm^{-1}, followed by a damping with a time constant of ∼2.5 ps. The latter two values are in excellent agreement with those obtained under 280-nm excitation (51). The GF of the entire dataset confirms these values, and the agreement with the experimental data is very satisfactory (Fig. 3 and *SI Appendix*, Fig. S2). Furthermore, we applied a Fourier analysis to the oscillatory parts of the datasets, after subtracting the exponential parts, as explained in *SI Appendix*, section SII. The fast Fourier transform maps showing the frequency as a function of probe wavelength are presented in *SI Appendix*, Fig. S3, and the reported frequencies for the S_0, S_1, and T_1 states are in excellent agreement with Table 1.

Because the decay of the S_1 state is reflected by the rise of the T_1 state, we attribute the 700- to 900-fs time constant to the $S_1 \rightarrow T_1$ ISC. The damping time of the S_1 wave packet of 1.1 ± 0.1 ps is longer than this ISC time but significantly shorter than the typical 1.7–2.5 ps (pure) dephasing time reported for the S_1 state of Pt(pop) in other solvents (Table 2) (40). In fact, the damping time of the singlet wave packet (Table 1) convolutes pure dephasing (or decoherence) with the ISC-mediated population decay. In the optical Bloch picture (41), the (measured) total dephasing rate is given by the following: $1/t_2 = 1/(2t_1) + 1/t_2^*$,

Table 1. Kinetic (exponential) times, τ_1– τ_3 and oscillation frequencies retrieved from a global fit of the data (*SI Appendix*, section SI.3) of Pt(pop) in MeCN

	λ_{exc}, nm	
Parameters	360	280
τ_1, fs	700 ± 100	280 ± 30
τ_2, ps	3.8 ± 0.4	3.5 ± 0.3
τ_3, ps	500	500
ω_G, cm^{-1}	119 ± 1	
τ_D^G, ps	2.2 ± 0.2	
ω_S, cm^{-1}	149 ± 1	
τ_D^S, ps	1.1 ± 0.1	
ω_T, cm^{-1}	157 ± 1	157 ± 1
τ_R^T, fs	900 ± 100	
τ_D^T, ps	2.5 ± 0.4	2.5 ± 0.3

τ_3 is fixed, and it corresponds to the long-lived $^3A_{2u}$ signals. Parameters retrieved from the oscillatory parts. $\omega_{G,S,T}$ and τ_D^G, τ_D^S, and τ_D^T are, respectively, the Pt–Pt wave packet oscillation frequency and its dephasing time in the singlet ground (G), singlet (S) $^1A_{2u}$, and triplet (T) $^3A_{2u}$ states. τ_R^T corresponds to the rise time of the Pt–Pt oscillations amplitude in the triplet state. The results for 280-nm excitation are from ref. 51.

Table 2. ISC times and wave packet damping times of the singlet and triplet states of diplatinum complexes in solution

Molecule/solvent	τ_{ISC}, ps	τ_D^S, ps	τ_D^T, ps
Pt(pop)/MeCN (this work)	0.7–0.9	1.10 (0.1)	2.5 (0.4)
Pt(pop)/DMF (40)	11.0 (0.1)	1.75 (0.08)	—
Pt(pop)/H_2O (40)	13.7 (0.2)	1.76 (0.08)	
Pt(pop)/EtOH (40)	25.6 (0.2)	2.30 (0.08)	—
Pt(pop)/Et-Gly (40)	30.3 (0.2)	1.93 (0.04)	—
Pt(pop)/H_2O-glycerol (1:2) (53)	40		
[Pt(ppy)(μ-^{t}Bu2pz)]2/toluene (49)	0.145		2.4
[Pt(pop) + 2H]$^{2-}$ (67)	0.68 (0.1)		

Columns 2–4, numbers in parentheses are uncertainties; column 1, numbers in parentheses are references. T_{ISC}, ISC times.

where t_1 is the population decay (here, the ISC time of 700–900 fs) time and t_2* is the pure dephasing time (1.7–2.5 ps in all solvents; Table 2). With these values, one arrives at t_2 = 0.96–1.28 ps, which compares favorably with the measured value of 1.1 ± 0.1 ps. The transfer of coherence is possible because the decoherence time (~2 ps) is two to three times longer than the ISC time. In all other solvents, the ISC time was 4–12 times longer than the decoherence time (40), so that the coherence is lost well before the ISC occurs.

The GF allows extracting the decay-associated spectra (DASs), which are shown in *SI Appendix*, Fig. S4. The 500- and 3.8-ps DASs are identical to those reported for the T_1 state under 280-nm excitation (51), reflecting similar decay and vibrational cooling processes. The 700-fs DAS exhibits a broad negative component between 470 and 550 nm, which is red-shifted with respect to the 500-ps DAS. This reflects the fact that, upon ISC, the T_1 state is populated in high vibrational levels. It also shows an additional minimum at 420 nm, which is due to the SE signal and a maximum at ~450 nm, which corresponds to the S_1 state ESA (Fig. 2) (40). Thus, this DAS captures all of the signals that characterize the kinetic evolution of the S_1 state.

While the solvent effect on the vertical excitation energies of the S_1 and T_1 states (*SI Appendix*, Fig. S1 and Table S2) is not significant, the marked solvent-dependent $S_1 \rightarrow T_1$ ISC rate seems to qualitatively correlate with the shifts of the UV bands with respect to the S_1 and T_1 states (*SI Appendix*, Table S2), that is, the redder the UV bands, the faster the ISC. However, although the UV bands in DMF and MeCN are the red-most shifted and lie at virtually the same energy (*SI Appendix*, Fig. S1 and Table S2), MeCN still shows an order of magnitude faster ISC than DMF (<1 vs. 11 ps).

These significant solvent effects on the ISC rate suggest that an additional state (or states) may be mediating the ISC from S_1 to T_1. This was already suggested by Milder and Brunschwig (53), who interpreted the temperature dependence of the picosecond S_1 fluorescence in frozen H_2O:glycerol matrices as being due to ISC via an intermediate primarily triplet ligand field (LF) state, and they estimated the barrier between the S_1 and this state to be in the 1,200–1,900 cm^{-1} range. The extremely fast relaxation channel to the T_1 state we recently reported upon 280-nm excitation of Pt(pop) and which bypasses the S_1 state (51), strongly supports the presence of a predominantly triplet state(s) that lie in the same region as the S_1 state and maybe the one(s) mediating the $S_1 \rightarrow T_1$ ISC. The above considerations suggest that the lower these intermediate state(s), the faster the ISC. However, as we show hereafter, the intermediate state is not LF as suggested in ref. 53.

The TDDFT calculations (with implicit solvent) (62) at the S_0 and S_1 state geometries report an energy gap between the S_1 state and next higher states, which is far too large (~4,000 cm^{-1}) to account for the ISC activation energies (53). This shows that the use of an implicit solvent is not sufficient to rationalize the present observations, and it calls for an explicit description of the solvent. Indeed, using QM/MM MD simulations, we rationalize the observations as described hereafter.

In these simulations, the QM part (the metal complex) is treated at the B3LYP/DFT/TDDFT level of theory (for details, see *SI Appendix*, section SIII). To assess the quality of the method, we computed the absorption spectrum of the system using structures sampled along a GS MD trajectory simulated in the NVT (canonical) ensemble at 300 K. The experimental singlet absorption band is compared with the simulated one in *SI Appendix*, Fig. S5, for the MeCN and EtOH solvents. Considering the approximations used in the dynamics (classical nuclei, QM/MM interface between the complex and the solvent, and the limited sampling), the agreement between the two is very good (with a red shift of the theoretical spectra of about 0.1–0.2 eV), justifying the use of this approach for the further analysis of the ES properties and dynamics. The extra structures of the theoretical spectra (high- and low-energy shoulders) are related to the classical nature of the Pt–Pt bond vibration that leads to an enhancement of the expectation values at the turning points and therefore to sidebands in the simulated absorption profile (64).

Fig. 4 shows the HOMO-1 to LUMO+2 Kohn–Sham (KS) orbitals computed for the GS optimized (minimum energy) geometry (upper line) and for two other structures taken from the dynamics in the T_1 state at 600 and 1,800 fs after their initiation (second and third line, respectively). It is clear from this figure that the orbitals are strongly distorted as a result of strong mixing of the GS-optimized orbitals in the ES and that this mixing evolves with time. *SI Appendix*, Table S3 shows the state energies and associated character composition of the lowest singlet and triplet states in MeCN calculated 600 and 1,800 fs after photoexcitation. The S_1 and T_1 states are populated by a transition from the HOMO to the LUMO, while the T_2 state(s) are from the HOMO to the mixed-character unoccupied KS orbitals (*SI Appendix*, Tables S3 and S4). It is important to note that, due to the mixing of orbitals in our explicit solvent calculations, the symmetry-based labeling and ES characters are no longer applicable in the course of ES evolution. For this reason, we label the ESs according to their energy ordering (*SI Appendix*, Table S3). The energy ordering and spatial distribution of the frontier orbitals in the S_1 (T_1) and T_2 states is induced by time-dependent local interactions of the excited molecule with the solvent molecules, in the course of the dynamics. In particular, the HOMO conserves its dσ* character (*SI Appendix*, Table S4), while the first three unoccupied orbitals become a linear combination of the LUMO, LUMO+1, and LUMO+2 orbitals of the optimized GS structure (Fig. 4, first line). Notably, the LUMO+1 and LUMO+2 solvent-exposed orbitals of the optimized structure (62) are distorted by the effect of the solvent.

To illustrate the effect of the strong solvation of the T_2 state(s), *SI Appendix*, Fig. S6 shows the time evolution of the S_1 and T_2 state energies as well as of the Pt–Pt bond along a trajectory

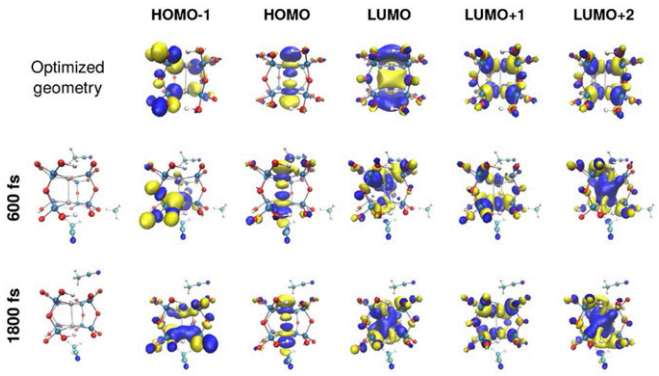

Fig. 4. Frontier orbital isosurfaces (isovalue of 0.025) of the optimized GS in acetonitrile (using the COSMO model for solvation) and of two frames selected from the ES dynamics in state T_1 at times 600 and 1,800 fs. Details are given in *SI Appendix*, section SIII.

propagated in the $T_1(S_1)$ state, for two different solvents: (*i*) acetonitrile and (*ii*) ethanol. The aim of this figure is by no means to quantitatively account for the experimental ISC rates but to qualitatively show the trends. Indeed, only a single trajectory was simulated for each solvent due to the computational cost of the QM/MM simulations; therefore, the present calculations lack statistical averaging (which would require several tens of simulations to be significant). In *SI Appendix*, Fig. S6, the amplitude of the energy fluctuations of the S_1 and T_2 state is large (typically, 0.5 eV), but the most important result is that the average energy of the T_2 state(s) and their molecular orbital representations (Fig. 4 and *SI Appendix*, Table S3) depart considerably from the ones obtained for the GS optimized structures with an implicit solvent (62). As a consequence of the dynamical interaction between the electronically excited complex and the solvent, a strong mixing of the high-lying LMMCT ESs occurs, which leads to a significant lowering of the corresponding state energies. Notably, the highly symmetric states labeled d^3A_u, b^3A_g, d^1A_u, and b^1A_g in ref. 62 (characterized by excitations from the predominantly metal dσ* orbital to pop-delocalized orbitals) are replaced in the fluctuating explicit solvent by states arising from asymmetric orbital mixing (differently stabilized by the solvent). As a consequence, the mixed-character T_2 state(s) occasionally cross the S_1 state in the course of the ES dynamics (*SI Appendix*, Fig. S6). These points of energy degeneracy, along with the large SOC constants (100–500 cm^{-1}) between the S_1 and T_2 states, favor ISC. However, extensive statistical sampling would be needed to relate the frequency of crossing events to the significantly different ISC rates in EtOH and MeCN.

To get further insight into the origin of the solvent effects on the ISC, we plot in *SI Appendix*, Fig. S8 the ES radial distribution functions (RdFs) of the H, C, and N (in MeCN) and H, O, and C (in EtOH) atoms with respect to the bridging (O_b) and the polar (O_p) oxygen atoms (defined in *SI Appendix*, Fig. S9). These data show that the solvent H atoms preferentially point toward the O_b atoms, while the N (of MeCN) and O (of EtOH) distributions peak at larger distances. The coordination numbers for all atomic species (radial integration of the RdF) are also shown (dot-dashed traces). The presence of an H peak below 2 Å in the EtOH RdF suggests the formation of a radially arranged pseudo–H-bond network between solute and solvent molecules. Indeed, in the case of MeCN, the RdF for the H atoms has its first maximum above 2 Å, and it is significantly broader than its equivalent in EtOH, suggesting a more labile solvation shell. The same applies to the RdF of the neighboring C atoms. These trends are more visible in the case of the RdFs measured from the O_ps. The case of EtOH shows a well-defined first solvation shell (*SI Appendix*, Fig. S10), while in MeCN no clear solvent structure is observed. Very recently, Møller and coworkers (65) reported calculations of the water solvent structure around Pt(pop) and presented RdFs that bear strong resemblance to those of EtOH in *SI Appendix*, Fig. S8. The ISC time in water is 13.7 ps (40), and the fact that the solvation shell shows, like EtOH, a higher degree of order than MeCN suggests that the higher disorder in the latter favors mixing and solvation of the higher LMMCT states and thus a faster ISC. It is also interesting to note that the $[Pt_2(\mu\text{-}P_2O_5(BF_2)_2)_4]^{4-}$ compound, with an electronic structure similar to Pt(pop) but a much more rigid ligand cage, exhibits an S_1 lifetime of 1.6 ns (63), orders of magnitude longer that Pt(pop). Thus, there seems to be a connection between the ligand/solvation shell structure and the mixing and solvation of the LMMCT states, which calls for further theoretical studies.

Pt(pop) is unstable in the gas phase, but the protonated $[Pt(pop) + 2H]^{2-}$ anionic species is stable and was recently characterized by mass spectrometry and time-resolved pump-probe photoelectron spectroscopy (66, 67). This species exhibits the same absorption bands as Pt(pop) in solution, suggesting very similar energetics of the lowest triplet and singlet states, but also of the higher-lying UV bands. Ultrafast experiments (67) showed that the S_1 state undergoes a decay accompanied by a concomitant rise in population of the T_1 state with the same rate as the ISC in MeCN. While this may be fortuitous, it does raise an interesting question. In $[Pt(pop) + 2H]^{2-}$, the two protons were calculated to be coordinated with polar oxygens at both ends of the molecule (see figure 2 of ref. 66), leading to a significant lowering of the molecular symmetry. While this would favor mixing of ESs, it may also suggest that a kind of microsolvation; mainly targeting the O_p atoms is sufficient to strongly affect the energetics of the intermediate T_2 state(s) and open the fast channel for ISC. In MeCN, the probability of symmetry lowering is higher due to a less structured solvation shell and so would also be the case of solvating dynamically the ES upon interaction with the polar oxygens. An alternative explanation for the gas phase results is that symmetry breaking is introduced by the two protons, which may simply make the ISC allowed between the S_1 and T_1 states, but considering their nested potential curves this seems unlikely.

As mentioned in the Introduction, several cases of ultrafast ISC in transition metal complexes have been reported (2, 34–38, 49), but whenever vibrational wave packets appeared, they were exclusively observed in the final state of different spin. The results presented here show a clearcut transfer of vibrational coherence during an ISC event, which underscores the importance of solvent effects in intramolecular dynamics. The experimental data show that the wave packet created in the S_1 state (with a frequency of 150 cm^{-1}) is coherently transferred to the T_1 state (157 cm^{-1}) over several oscillation cycles. It is remarkable that the wave packet frequency increases after this transfer. However, this can be understood considering that a wave packet is a coherent superposition of several vibrational wave functions with a certain energy spread, determined by the pump laser spectral width, in the present case ∼550 cm^{-1}, that is, it spans three to four vibrational levels of both S_1 and T_1. This and the very close vibrational frequencies in the two electronic states make it possible to have a vibrational coherence appearing in the T_1 state.

The present case of ultrafast ISC induced by the mixing and solvation of states that mediate the spin change is different from the case reported in refs. 68 and 69, where coherence transfer occurs in an ultrafast ISC event in the ClF molecule trapped in rare gas matrices. In the latter, excitation of the dissociative $^1\Pi_1$ state leads to the vibrational wave packet switching to the bound $^3\Pi$ state in <0.5 ps. This ultrafast spin flip is due to coherent caging of the fragments by the matrix at the asymptotic limit where singlet and triplet state are nearly degenerate, thus compensating for the weak SOC constant.

The picture that emerges from the present experimental and theoretical results is schematically shown in Fig. 1, where the T_2 state(s) depicted with red dashed line is (are) those that mediate the ISC but probably also cause the direct population of the triplet state upon UV excitation reported in ref. 51. The energy of the T_2 intermediate state(s) is determined by the solvent. The QM/MM simulations show how differential shifts and mixings of molecular ESs due to dynamical solvent effects (fluctuations) can induce new relaxation channels. This is of importance in photochemistry as large polyatomic molecules consist of various types of states: valence, charge transfer, or Rydberg, which have largely different interactions with their environment such that the respective intramolecular potential surfaces can be strongly shifted and their crossing points, for example, at conical intersections, can end up strongly modified.

Conclusions

We reported on the transfer of vibrational coherence from a singlet to a triplet state in an ultrafast ISC induced by the solvent environment. Our results show an ISC on the timescale of 0.7–0.9 ps from the S_1 to the T_1 state in acetonitrile, ∼10–30 times faster than in other solvents (40, 53). We rationalize the observation of coherence transfer on the basis of the following: (*i*) the $S_1(^1A_{2u}) \rightarrow T_1(^3A_{2u})$ ISC time (∼0.7 ps) is faster than the decoherence time of the wave packet in the singlet and triplet states (typically 1.7–2.5 ps), so that coherence is preserved during and after ISC; (*ii*) an intermediate state (or group of states, labeled T_2) is mediating the ISC, whose existence is inferred from QM/MM MD simulations. These states, of predominantly triplet

character, result from the solvent-induced dynamic mixing and strong solvation of higher lying LMMCT states, so that in MeCN they are degenerate with the S_1 state; (*iii*) the MD simulations also suggest that symmetry breaking may be crucial for the acceleration of the ISC, as the solvation shell is much more structured in EtOH and H_2O (slow ISC) compared with MeCN (fast ISC).

ACKNOWLEDGMENTS. This work was supported by the Swiss National Science Foundation (NSF) via the National Center of Competence in Research/ Molecular Ultrafast Science and Technology and Contract 200021_137717. We also thank the European collaboration program Cooperation in Science and Technology (Actions CM1202 and CM1405), the Czech Science Foundation (Grant 17-011375), and the NSF Center for Chemical Innovation in Solar Fuels Program (CHE-1305124) for support.

1. Zewail AH (2000) Femtochemistry: Atomic-scale dynamics of the chemical bond using ultrafast lasers (Nobel lecture). *Angew Chem Int Ed Engl* 39:2586–2631.
2. Chergui M (2015) Ultrafast photophysics of transition metal complexes. *Acc Chem Res* 48:801–808.
3. Dantus M, Bowman RM, Gruebele M, Zewail AH (1989) Femtosecond real-time probing of reactions. 5. The reaction of Ihgi. *J Chem Phys* 91:7437–7450.
4. Rose TS, Rosker MJ, Zewail AH (1989) Femtosecond real-time probing of reactions. 4. The reactions of alkali-halides. *J Chem Phys* 91:7415–7436.
5. Zewail AH (2000) Femtochemistry: Atomic-scale dynamics of the chemical bond. *J Phys Chem A* 104:5660–5694.
6. Szarka AZ, Pugliano N, Palit DK, Hochstrasser RM (1995) Vibrational coherence in the solution-phase photoisomerization reaction of *cis*-stilbene. *Chem Phys Lett* 240:25–30.
7. Volk M, et al. (1997) Anisotropy measurements of solvated HgI_2 dissociation: Transition state and fragment rotational dynamics. *J Phys Chem A* 101:638–643.
8. Voth GA, Hochstrasser RM (1996) Transition state dynamics and relaxation processes in solutions: A frontier of physical chemistry. *J Phys Chem* 100:13034–13049.
9. Cina JA, Fleming GR (2004) Vibrational coherence transfer and trapping as sources for long-lived quantum beats in polarized emission from energy transfer complexes. *J Phys Chem A* 108:11196–11208.
10. Scherer NF, Jonas DM, Fleming GR (1993) Femtosecond wave-packet and chemical-reaction dynamics of iodine in solution—tunable probe study of motion along the reaction coordinate. *J Chem Phys* 99:153–168.
11. Apkarian VA, Schwentner N (1999) Molecular photodynamics in rare gas solids. *Chem Rev* 99:1481–1514.
12. Cong P, Roberts G, Herek JL, Mohktari A, Zewail AH (1996) Femtosecond real-time probing of reactions. 18. Experimental and theoretical mapping of trajectories and potentials in the NaI dissociation reaction. *J Phys Chem* 100:7832–7848.
13. Dhar L, Rogers JA, Nelson KA (1994) Time-resolved vibrational spectroscopy in the impulsive limit. *Chem Rev* 94:157–193.
14. Banin U, Waldman A, Ruhman S (1992) Ultrafast photodissociation of I_3^- in solution—direct observation of coherent product vibrations. *J Chem Phys* 96:2416–2419.
15. Banin U, Ruhman S (1993) Ultrafast vibrational dynamics of nascent diiodide fragments studied by femtosecond transient resonance impulsive stimulated Raman-scattering. *J Chem Phys* 99:9318–9321.
16. Pugliano N, Gnanakaran S, Hochstrasser RM (1996) The dynamics of photodissociation reactions in solution. *J Photoch Photobio A* 102:21–28.
17. Rosca F, et al. (2000) Investigations of coherent vibrational oscillations in myoglobin. *J Phys Chem A* 104:4280–4290.
18. Bursing H, Vohringer P (2000) Transition state probing and fragment rotational dynamics following impulsive bond breakage of HgI_2. *Phys Chem Chem Phys* 2:73–82.
19. Hess S, Bursing H, Vohringer P (1999) Dynamics of fragment recoil in the femtosecond photodissociation of triiodide ions in liquid solution. *J Chem Phys* 111:5461–5473.
20. Lenderink E, Duppen K, Wiersma DA (1995) Femtosecond twisting and coherent vibrational motion in the excited-state of tetraphenylethylene. *J Phys Chem* 99: 8972–8977.
21. Wang Q, Schoenlein RW, Peteanu LA, Mathies RA, Shank CV (1994) Vibrationally coherent photochemistry in the femtosecond primary event of vision. *Science* 266: 422–424.
22. Kobayashi T, Saito T, Ohtani H (2001) Real-time spectroscopy of transition states in bacteriorhodopsin during retinal isomerization. *Nature* 414:531–534.
23. Polli D, et al. (2010) Conical intersection dynamics of the primary photoisomerization event in vision. *Nature* 467:440–443.
24. Schenkl S, et al. (2006) Insights into excited-state and isomerization dynamics of bacteriorhodopsin from ultrafast transient UV absorption. *Proc Natl Acad Sci USA* 103:4101–4106.
25. Zgrablic G, Haacke S, Chergui M (2007) Vibrational coherences of the protonated Schiff base of all-trans retinal in solution. *Chem Phys* 338:168–174.
26. Briand J, et al. (2010) Coherent ultrafast torsional motion and isomerization of a biomimetic dipolar photoswitch. *Phys Chem Chem Phys* 12:3178–3187.
27. Takeuchi S, Tahara T (2005) Coherent nuclear wavepacket motions in ultrafast excited-state intramolecular proton transfer: Sub-30-fs resolved pump-probe absorption spectroscopy of 10-hydroxybenzo[*h*]quinoline in solution. *J Phys Chem A* 109:10199–10207.
28. Fuji T, Ong HJ, Kobayashi T (2003) Real-time observation of vibrational coherence persisting after internal conversion and vibrational relaxation in cyanine dye molecules. *Chem Phys Lett* 380:135–140.
29. Braem O, Penfold TJ, Cannizzo A, Chergui M (2012) A femtosecond fluorescence study of vibrational relaxation and cooling dynamics of UV dyes. *Phys Chem Chem Phys* 14: 3513–3519.
30. Nakashima S, et al. (2000) Coherent dynamics in ultrafast charge-transfer reaction of plastocyanin. *Chem Phys Lett* 331:396–402.
31. Egorova D, Domcke W (2004) Quantum dynamical simulations of ultrafast photoinduced electron-transfer processes. *J Photoch Photobio A* 166:19–31.
32. Wynne K, Reid GD, Hochstrasser RM (1996) Vibrational coherence in electron transfer: The tetracyanoethylene-pyrene complex. *J Chem Phys* 105:2287–2297.
33. Gonzalez CR, Fernandez-Alberti S, Echave J, Chergui M (2002) Vibrational coherence and nonadiabatic dynamics in the condensed phase. *J Chem Phys* 116:3343–3352.
34. Consani C, et al. (2009) Vibrational coherences and relaxation in the high-spin state of aqueous $[Fe^{II}(bpy)_3]^{2+}$. *Angew Chem Int Ed Engl* 48:7184–7187.
35. Auböck G, Chergui M (2015) Sub-50-fs photoinduced spin crossover in $[Fe(bpy)_3]^{2+}$. *Nat Chem* 7:629–633.
36. Schrauben JN, Dillman KL, Beck WF, McCusker JK (2010) Vibrational coherence in the excited state dynamics of Cr(acac)(3): Probing the reaction coordinate for ultrafast intersystem crossing. *Chem Sci (Camb)* 1:405–410.
37. Iwamura M, Nozaki K, Takeuchi S, Tahara T (2013) Real-time observation of tight Au-Au bond formation and relevant coherent motion upon photoexcitation of $[Au(CN)_2^-]$ oligomers. *J Am Chem Soc* 135:538–541.
38. Iwamura M, et al. (2016) Coherent vibration and ultrafast dynamics upon bond formation in excited dimers of an Au(I) complex. *Phys Chem Chem Phys* 18:5103–5107.
39. Auböck G, et al. (2012) Femtosecond pump/supercontinuum-probe setup with 20 kHz repetition rate. *Rev Sci Instrum* 83:093105.
40. van der Veen RM, Cannizzo A, van Mourik F, Vlček A, Jr, Chergui M (2011) Vibrational relaxation and intersystem crossing of binuclear metal complexes in solution. *J Am Chem Soc* 133:305–315.
41. Jean JM, Fleming GR (1995) Competition between energy and phase relaxation in electronic curve crossing processes. *J Chem Phys* 103:2092–2101.
42. Gray HB, Záliš S, Vlček A (2017) Electronic structures and photophysics of d8-d8 complexes. *Coord Chem Rev* 345:297–317.
43. Fordyce WA, Brummer JG, Crosby GA (1981) Electronic spectroscopy of a diplatinum(Ii) octaphosphite complex. *J Am Chem Soc* 103:7061–7064.
44. Rice SF, Gray HB (1983) Electronic absorption and emission-spectra of binuclear platinum(Ii) complexes–Characterization of the lowest singlet and triplet excited-states of Pt2(H2p2o5)44-. *J Am Chem Soc* 105:4571–4575.
45. Stiegman AE, Rice SF, Gray HB, Miskowski VM (1987) Electronic spectroscopy of D8-D8 diplatinum complexes–1a2u(Dsigma star-]P-sigma), 3eu(Dxz,Dyz-]P-Sigma), and 3,1b2u(Dsigma star-] Dx2-Y2) excited-states of Pt2(P2o5h2)44-. *Inorg Chem* 26: 1112–1116.
46. van der Veen RM, et al. (2009) Structural determination of a photochemically active diplatinum molecule by time-resolved EXAFS spectroscopy. *Angew Chem Int Ed Engl* 48:2711–2714.
47. van der Veen RM, et al. (2010) L-edge XANES analysis of photoexcited metal complexes in solution. *Phys Chem Chem Phys* 12:5551–5561.
48. Christensen M, et al. (2009) Time-resolved X-ray scattering of an electronically excited state in solution. Structure of the 3A(2u) state of tetrakis-mu-pyrophosphitodiplatinate(II). *J Am Chem Soc* 131:502–508.
49. Cho S, et al. (2011) Coherence in metal-metal-to-ligand-charge-transfer excited states of a dimetallic complex investigated by ultrafast transient absorption anisotropy. *J Phys Chem A* 115:3990–3996.
50. Hartsock RW, Zhang W, Hill MG, Sabat B, Gaffney KJ (2011) Characterizing the deformational isomers of bimetallic $Ir_2(dimen)_4^{2+}$ (dimen = 1,8-diisocyano-*p*-menthane) with vibrational wavepacket dynamics. *J Phys Chem A* 115:2920–2926.
51. Monni R, et al. (2017) Conservation of vibrational coherence in ultrafast electronic relaxation: The case of diplatinum complexes in solution. *Chem Phys Lett* 683: 112–121.
52. Roundhill DM, Gray HB, Che CM (1989) Pyrophosphito-bridged diplatinum chemistry. *Acc Chem Res* 22:55–61.
53. Milder SJ, Brunschwig BS (1992) Factors affecting nonradiative decay–Temperature-dependence of the picosecond fluorescence lifetime of Pt2(Pop)4(4-). *J Phys Chem* 96: 2189–2196.
54. Auböck G, Consani C, van Mourik F, Chergui M (2012) Ultrabroadband femtosecond two-dimensional ultraviolet transient absorption. *Opt Lett* 37:2337–2339.
55. Moret ME, Tavernelli I, Rothlisberger U (2009) Combined QM/MM and classical molecular dynamics study of $[Ru(bpy)_3]^{2+}$ in water. *J Phys Chem B* 113:7737–7744.
56. Tavernelli I, Curchod BFE, Rothlisberger U (2011) Nonadiabatic molecular dynamics with solvent effects: A LR-TDDFT QM/MM study of ruthenium (II) tris (bipyridine) in water. *Chem Phys* 391:101–109.
57. Curchod BFE, Rothlisberger U, Tavernelli I (2013) Trajectory-based nonadiabatic dynamics with time-dependent density functional theory. *ChemPhysChem* 14: 1314–1340.
58. von Lilienfeld OA, Tavernelli I, Rothlisberger U, Sebastiani D (2004) Optimization of effective atom centered potentials for london dispersion forces in density functional theory. *Phys Rev Lett* 93:153004.
59. von Lilienfeld OA, Tavernelli I, Rothlisberger U, Sebastiani D (2005) Performance of optimized atom-centered potentials for weakly bonded systems using density functional theory. *Phys Rev B* 71:195119.
60. Lin IC, et al. (2007) Library of dispersion-corrected atom-centered potentials for generalized gradient approximation functionals: Elements H, C, N, O, He, Ne, Ar, and Kr. *Phys Rev B* 75:205131.

61. Wang F, Ziegler T (2004) Excitation energies of some d(1) systems calculated using time-dependent density functional theory: An implementation of open-shell TDDFT theory for doublet-doublet excitations. *Mol Phys* 102:2585–2595.
62. Záliš S, Lam YC, Gray HB, Vlček A (2015) Spin-orbit TDDFT electronic structure of diplatinum(II,II) complexes. *Inorg Chem* 54:3491–3500.
63. Durrell AC, et al. (2012) Structural control of 1A2u-to-3A2u intersystem crossing in diplatinum(II,II) complexes. *J Am Chem Soc* 134:14201–14207.
64. Bergsma JP, Berens PH, Wilson KR, Fredkin DR, Heller EJ (1984) Electronic spectra from molecular dynamics: A simple approach. *J Phys Chem* 88:612–619.
65. Levi G, Pápai M, Henriksen NE, Dohn AO, Møller KB (2018) Solution structure and ultrafast vibrational relaxation of the PtPOP complex revealed by ΔSCF-QM/MM direct dynamics simulations. *J Phys Chem C* 122:7100–7119.
66. Kruppa SV, et al. (2016) Fragmentation pathways of dianionic $[Pt_2(\mu\text{-}P_2O_5H_2)_4 + X,Y]^{2-}$ (X,Y = H, K, Ag) species in an ion trap induced by collisions and UV photoexcitation. *Int J Mass Spectrom* 395:7–19.
67. Winghart M-O, et al. (2016) Time-resolved photoelectron spectroscopy of a dinuclear Pt(II) complex: Tunneling autodetachment from both singlet and triplet excited states of a molecular dianion. *J Chem Phys* 144:054305.
68. Bargheer M, Niv MY, Gerber RB, Schwentner N (2002) Ultrafast solvent-induced spin-flip and nonadiabatic coupling: ClF in argon solids. *Phys Rev Lett* 89:108301.
69. Bargheer M, et al. (2007) Dynamics of electronic states and spin-flip for photodissociation of dihalogens in matrices: Experiment and semiclassical surface-hopping and quantum model simulations for F_2 and ClF in solid Ar. *J Phys Chem A* 111:9573–9585.